Instrumented Impact Property and Fracture Process Behavior of Composite Rubber Toughened ABS Terpolymer

Zhisheng Yu,[1,2] Chaoxian Wang,[1,3] Yang Li,[1] Yurong Wang[1]

[1]Liaoning Province Key Laboratory of Polymer Science and Engineering, Faculty of Chemical, Environmental and Biological Science and Technology, Dalian University of Technology, Dalian 116024, People's Republic of China

[2]Sinopec Key Laboratory of Surfactants for EOR, Shanghai Research Institute of Petrochemical Technology, SINOPEC, Shanghai 201208, People's Republic of China

[3]Beijing Chemical Industry Institute Yanshan Branch, SINOPEC, Beijing 102500, People's Republic of China

Correspondence to: Y. Li (E-mail: liyang@dlut.edu.cn)

ABSTRACT: A series of low-*cis*-1,4/high-*cis*-1,4 polybutadiene composite rubber toughened poly(acrylonitrile-butadiene-styrene) (ABS) terpolymers were prepared and characterized. The morphological analysis shows that specimens exhibit common characteristics of two single rubbers while mechanical measurements reveal that better comprehensive properties can be obtained as more Ni-9004 blended in composite rubber. When increasing Ni-9004/Li-700A ratio, one brittle–ductile transition occurs at 5.0 wt % rubber usage and three transition regions exist under 10.0 wt % usage. In addition, the characteristic force–time curves and fractography demonstrate that failure behavior and crack propagation mode can be effectively evaluated. Conclusively, quasi-brittle fracture can be seen for specimens with obvious cavitation and matrix stripping followed by riverlike fibrous and periodical Wallner stripes, whereas ductile fracture is observed for those with alternate parabolic and firework patterns accompanying stress-whitening and ligament-forming progress. © 2012 Wiley Periodicals, Inc. J. Appl. Polym. Sci. 000: 000–000, 2012

INTRODUCTION

Due to leaps from qualitative to quantitative evaluation, instrumented impact tests have been extensively applied in industrial production and scientific research for assessing the impact fracture characteristics and fracture mechanics parameters of different toughened thermoplastics.[1,2] The tests not only yield much more complete representations of an impact than a single calculated value but also allow both the independent consideration of different energy components (elastic and plastic deformation energy, crack propagation energy, etc.) involved during the process of crack growth, and the separate evaluation of resistance against stable crack initiation, stable, or unstable crack propagation.[3] They are also useful in simulating functional impact resistance and in running material comparisons. The instrumented pendulum or drop weight testing emerges as the times require and is considered to be presently the best general impact testing method available.

A comparison of instrumented Charpy and Izod test modes for polystyrene (PS) has been performed and showed that two results could be directly compared independent of fracture mode.[4,5] It is not unique that, Tai et al.[6] found that the instrumented Charpy impact results were slightly lower than the Izod ones and concluded that the impact type played an important role in the impact fracture behavior of polymer blends. Pick and Harkin-Jones[7] investigated the relationship between thermal relaxations and impact performance of rotationally molded LLDPE based on instrumented impact test and dynamic mechanical thermal analysis and found a correlation between changes in loss modulus and crack initiation energy with temperature and proposed a method for predicting impact performance over a wide temperature range. Effects of annealing and microstructure of glass fiber-reinforced polyphenylene sulfide on elastic deformation, crack formation, and crack propagation were also studied via instrumented impact tester.[8]

To obtain failure criteria of engineering specimens with cracks, various concepts of fracture mechanics in instrumented impact tests have been developed and proposed for different systems.[9] It was concluded that ductile deformation occurred in samples with shorter ligament lengths, whereas brittle failure prevailed in those with longer ones. Meanwhile, a progressive impact

fracture model was proposed by Cheon et al.[10] to analyze the dynamic fracture load and energy absorption characteristics during the impact progress. Besides, extrapolation of standard tensile stress–strain curves is another approach for determining the thermoplastics' behaviors in impact conditions.[11] A master stress–strain expression and an extrapolation law were established based on drop weight impact tests by implementing with finite element analysis software.[12]

On the other hand, as is known, the toughness of rubber-toughened thermoplastics significantly depends on the characteristic rubbery morphology, which is further affected by rubber type and content, particle diameter, interparticle distance, cavitation behavior, technical conditions and so on. Although rubber type is the most important factor among the foresaid factors, a single one rubber type basically endows the modified material with single or some aspects of excellent performances rather than comprehensive properties, for example, toughness, modulus, glossiness, and so on. So, it is of significance to investigate the influence of compounded rubber on toughness and fracture mechanisms. Although different rubber types in toughened thermoplastics (ABS) have been researched in previous studies,[13–18] limited analyses or pertinent reports on the fractography and fracture mechanism of compounded rubber systems under instrumented impact event have been undertaken. This article focuses on the investigation of fracture process behaviors and mechanisms of low-*cis*-1,4/high-*cis*-1,4 polybutadiene (PB) rubber cotoughened materials via instrumented Izod impact testing and morphological examination of fractured surfaces.

EXPERIMENTAL

Materials

High-*cis*-1,4 PB rubber (Ni-9004, 97.0 % of *cis* isomer, $\overline{M}_n = 81,000$, $\overline{M}_w/\overline{M}_n = 3.81$) was supplied by Beijing Yanshan, PetroChina. Low-*cis*-1,4 PB rubber (Li-700A, 32.3 % of *cis* isomer, $\overline{M}_n = 117,000$, $\overline{M}_w/\overline{M}_n = 1.40$) was obtained from Asahi Kasei, Japan. Acrylonitrile and styrene were supplied by Daqing Petrochemical, PetroChina and distilled under vacuum before use. 1,1-bis(*tert*-butylperoxy)cyclohexane (DP275B) as a difunctional initiator was purchased from Qiangsheng Chemical, China and used as received. Other solvents, for example, chloroform, ethylbenzene, methanol, and tetrahydrofuran, were purchased from Aldrich Chemical and used as received without further purification.

Synthesis and Preparation of Toughened Terpolymers

Details for the preparation of the various ABSs can be referred in a previous paper.[14] Briefly, rubber dissolution was performed in nitrogen atmosphere at room temperature for 12 h, and bulk polymerization was conducted for 4 h at 105°C with a stirring speed of 375 rpm and another 5 h at 150°C. The products were isolated by dissolving and precipitating method and then dried in a vacuum oven at 50°C for 48 h. Dumb-bell shaped specimens and impact specimens were injection-molded by RR3400 Model 2 Injection Test Sample Molding Apparatus (Ray-Ran, UK) and placed at room temperature for 48 h after molding.

Measurement and Characterization

Tensile Testing. Tensile testing was carried out following the ASTM D-638 using an INSTRON 5567 Universal Tensile Tester (US) at 23°C with a crosshead speed of 5.0 mm min^{-1}, an initial gaze length of 40.0 mm, and a cross section of 4.0 × 2.1 mm^2.

Notched Izod Impact Testing. According to ASTM D-256, notched specimens with the dimensions of 4.0 × 10.0 × 80.0 mm^3 were cut with a V-notch of 2.0 mm depth on the narrow side of the specimens by means of a CEAST 6951 notching machine (Italy). An instrumented Resile Impactor (CEAST 695606, Italy) with a maximum work capacity of 2.7 J was used at 23°C for fracture mechanics investigations. Signals from sensors of the tester were transferred to a Microsoft-PC by a Data Acquisition System (CEAST DAS4000, Italy). The nominal velocity of pendulum hammer was set to be 3.46 m s^{-1}, the used hammer mass was 0.46 kg, and the distance between contact point and notch center was 20.0 mm.

Transmission Electron Microscopy. Transmission electron microscopy (TEM) images of ABS samples were obtained with a TECNAI20 TEM (FEI, US) at an accelerating voltage of 200 kV. The as-prepared samples were first ultramicrotomed with a diamond knife on a LEICA ULTRACUT Ultramicrotome (Switzerland) at −120°C to produce ultrathin sections with a nominal thickness of 100 nm. Then, the sections were transferred from water to Cu grids of 200 mesh and stained with an OsO$_4$ solution at room temperature for 24 h to enhance the contrast between rubber and matrix before observation.

Scanning Electron Microscopy. Impact fracture surfaces of the specimens were coated with a thin gold layer on a K550X Sputtering Coater (EMITECH, UK) and then observed to analyze the fracture nature and deformation mechanism. Scanning electron microscopy (SEM) analysis was performed by a QUANTA200 SEM (FEI, US) using a working voltage of 20 kV.

RESULTS AND DISCUSSION

Characteristic Microstructure and Disperse Phase Morphology

The characteristics of the as-prepared terpolymers toughened by different Li-700A/Ni-9004 ratio and usage are tabulated in Table I. Figure 1 shows the typical TEM micrographs of samples toughened by different rubber usage and Ni-9004/Li-700A ratio. As our previous study, Li-700A toughened terpolymer had uniformly fine rubber particles with plenty of SAN subinclusions and relatively fuzzy two-phase interface, whereas Ni-9004 toughened product owned certain microsized irregular particles with heterogeneous distribution and relatively clear boundary.[14] As can be seen from Figure 1, all images display the common characteristics of Li-700A and Ni-9004. Larger Ni-9004 rubber particles and smaller Li-700A ones distribute alternately and dispersedly. In addition, not only the total volume fraction of rubber phase but also the dispersed particle size is accelerated with rubber usage improving, which is in good agreement with Tokita's theory and Jose' studies.[21] The increased particle size can be mainly attributed to (i) the increase in shear stress due to the enhancement in viscosity of the system, (ii) the increase

Table I. Mass Grafting Polymerization and Structural Parameters of ABS Terpolymers

	PB rubber			Grafting phase			Free SAN phase	
Sample[a]	Li-700A[b] (wt %)	Ni-9004[b] (wt %)	PB[c] (wt %)	GD[d] (%)	RPVF[e] (%)	Nt*[f]	$\overline{M}_n$[g] (10^{-5})	$\overline{M}_w/\overline{M}_n$[g]
ABS-1	100	0	5.0	502.7	37.9	4.03	1.46	1.98
ABS-2	75	25	5.0	454.3	35.6	2.96	1.67	1.82
ABS-3	50	50	5.0	412.7	34.5	2.28	1.79	1.60
ABS-4	25	75	5.0	380.4	32.4	1.70	2.04	1.87
ABS-5	0	100	5.0	361.1	31.8	1.85	1.58	1.68
ABS-6	100	0	10.0	267.3	56.8	3.68	0.85	1.84
ABS-7	75	25	10.0	263.7	55.1	3.30	0.87	1.96
ABS-8	50	50	10.0	221.0	49.3	2.35	0.93	2.07
ABS-9	25	75	10.0	204.0	44.3	2.21	0.84	1.73
ABS-10	0	100	10.0	208.7	46.8	1.86	0.91	1.95

[a]Containing approximately 23.0 % AN composite content characterized with FTIR analysis,[19] [b]Weight percentage content of single rubber in total compounded rubber usage, [c]Weight percentage content of total compounded rubber in the recipe, [d]Denoting the grafting degree of PB rubber, [e]Representing the volume fraction of rubber phase, [f]Nt* (grafting density) denoting the average number of branches per backbone of PB macromolecular chain estimated by a formula: $[SAN_{graft}/PB] \times [\overline{M}_{nPB}/\overline{M}_{nSANfree}]$,[20] [g]Measured by TDA302 SEC/LALS (Viscotek, US).

in coalescence because the number of dispersed particles and therefore the probability of particles colliding with each other increases, and (iii) the increase in the interfacial tension caused by the gradually depressed grafting degree and grafting density of rubber while its usage increases.

Moreover, due to the existence of higher molecular weight part in Ni-9004 with broader $\overline{M}_w/\overline{M}_n$, the size of dispersed particles increases with the Ni-9004/Li-700A ratio under any total rubber usage. At the same time, the number of larger particles is elevated due to much more Ni-9004 composition introduced into the compounded system. The critical variables in controlling particle breakup and distribution of dispersed phase during the processing of polymer blends are the droplet diameter, viscosity ratio of droplet phase to matrix, interfacial tension, and shear rate.[21] So, the final blend morphology is determined by the factors related to processing conditions and material parameters such as blend composition, viscosity ratio, elasticity ratio, interfacial tension, and so on. There is a balance between the deformation and disintegration phenomena and the coalescence of dispersed particles. Meanwhile, rubber-graft-SAN polymers *in situ* forming and existing in multiphase system can reduce the interfacial tension and thus result in a finer dispersion of phase and a better stability against coalescence. The accompanying improved interfacial adhesion among phases is also favorable to promote stress transfer via the interface.[22]

Evaluation of Mechanical Properties

The tensile stress–strain relationship curves, the relative tensile moduli, and the notched Izod impact strengths of rubber toughened materials with respect to the Ni-9004/Li-700A ratio under various total rubber usages are shown in Figure 2. As seen, all curves can be divided into two characteristic load regions: the elastic deformation region and the plastic deformation region [Figure 2(a)]. In the former stage, the tensile stress

shows linear increase with the strain quickly, whereas in the latter stage, an apparent strain-softening occurs, that is, the stress decreases to a certain degree with the strain increasing. The elongations at break of ABSs are remarkably enhanced while Ni-9004 content is higher in composite toughener and the total rubber usage is increased from 5.0 to 10.0 wt %. Meanwhile, the tensile moduli (the slope of the elastic region) increase slightly while more Ni-9004 amount is blended into the composite rubber; however, they are significantly reduced with increasing the total rubber usage. As also shown in Figure 2(b), compared to ABSs using pure Li-700A as modifier, the moduli of as-prepared products by Ni-9004 are increased approximately 7.6 and 0.8% for 5.0 and 10.0 wt % rubber system, respectively. The obtained results may be mainly due to the relatively lower modulus and stiffness of rubber domains than those of matrix and the insignificant difference between the two single rubbers.

Furthermore, considering the Izod impact values combined with the fracture mode, different brittle–ductile regions can be evaluated and speculated. In the case of 5.0 wt % rubber system, there exists an obvious enhancement in impact strength while the mixing ratio of rubber composite increases from 50 : 50 to 75 : 25 [Figure 2(c)]. Compared with ABS-3, a substantial increase in impact strength (~92.8%) of ABS-4 has occurred. The changing process is accompanied by a transition from the quasi-brittle failure mode to semiductile fracture mode of specimens. On the other hand, surprisingly, two transition points are presented in 10.0 wt % rubber system. One exists in a similar region to the 5.0 wt % rubber system; the other is in the Ni-9004/Li-700A proportion region of 0 : 100–25 : 75. In other words, at this level there are totally three regions (fracture mode): region I, semiductile mode; region II, ductile mode; and region III, super-tough mode. Besides, a somewhat inferior improvement in impact strengths of ABS-7 (~65.2%) and ABS-10 (~41.5%) can be obtained in contrast to ABS-6 and ABS-9,
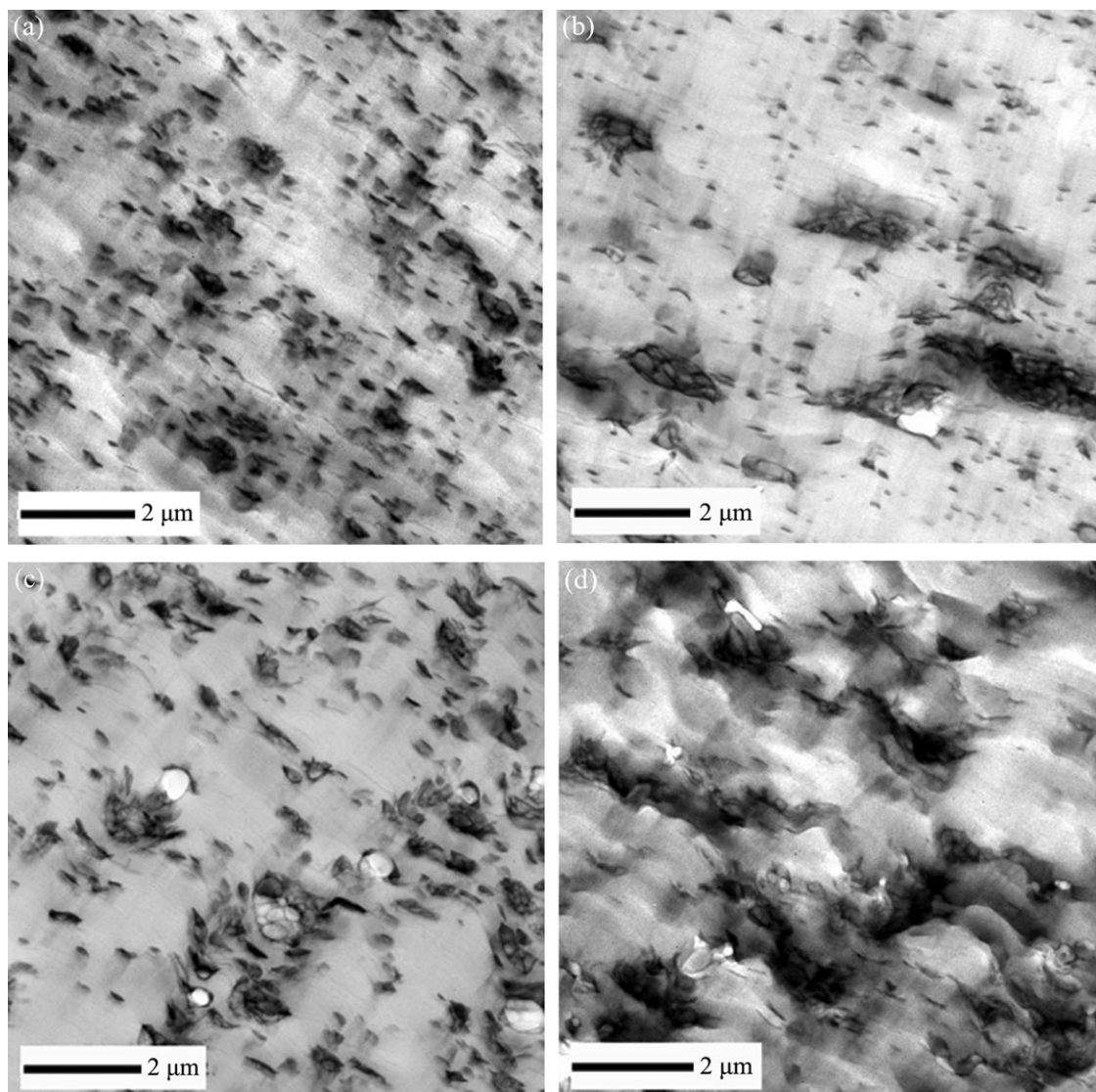
Figure 1. TEM micrographs (magnification ×2250) of (a) ABS-2, (b) ABS-4, (c) ABS-7, and (d) ABS-9.

respectively. These conclusions also coincide well with van der Wal's investigations.[1,23]

In a word, the anti-impact properties of toughened materials are greatly affected by rubber type and usage. The relatively better mechanical properties of ABS toughened by composite rubber or pure Ni-9004 rather than Li-700A may be attributed to the following three aspects: (i) the compound effect of a suitable amount of larger rubber particles; (ii) the orientation and deformability of *cis*-1,4 rubber chains during stretching; and (iii) the proper interfacial bonding force between rubber particles and matrix.

Characteristics of Instrumented Impact Curves
Figure 3 illustrates the typical force–time (*f–t*) curves of as-prepared thermoplastics under different rubber usages, which describe the high-rate impact behavior of specimens. As displayed, the arrow symbols along each curve stand for the inertial peak, maximum peak, and deflection where specimen

entirely or partially breaks, respectively. Several aspects of material properties can be inferred from the obtained *f–t* diagrams. The principal characteristic parameters, for example, inertial peak force (F_0), maximum impact force (F_{max}), deflection (d_{max}), time (t_{max}) and energy (W_{max}) at F_{max}, total absorbed energy (W_t), and so forth, were measured and summarized in Table II. The F_0 induced by contact mass can be regarded as the response of materials to hammer and therefore, a preliminary evaluation of stiffness and modulus. The more rigid or stiffer a material is, the higher its modulus and stiffness is, and the greater the F_0 under instrumented impact is. Table II shows a roughly increasing trend of F_0 values with increasing Ni-9004 amount in compound rubber. And this trend becomes more obviously at higher rubber usage because of the greatest difference in moduli of ABS with different compounded rubber [Figure 2(b)]. On the other hand, F_0 tends to higher with a decrease in total rubber usage considerably attributed to the high strength and low flexibility of the toughened products.
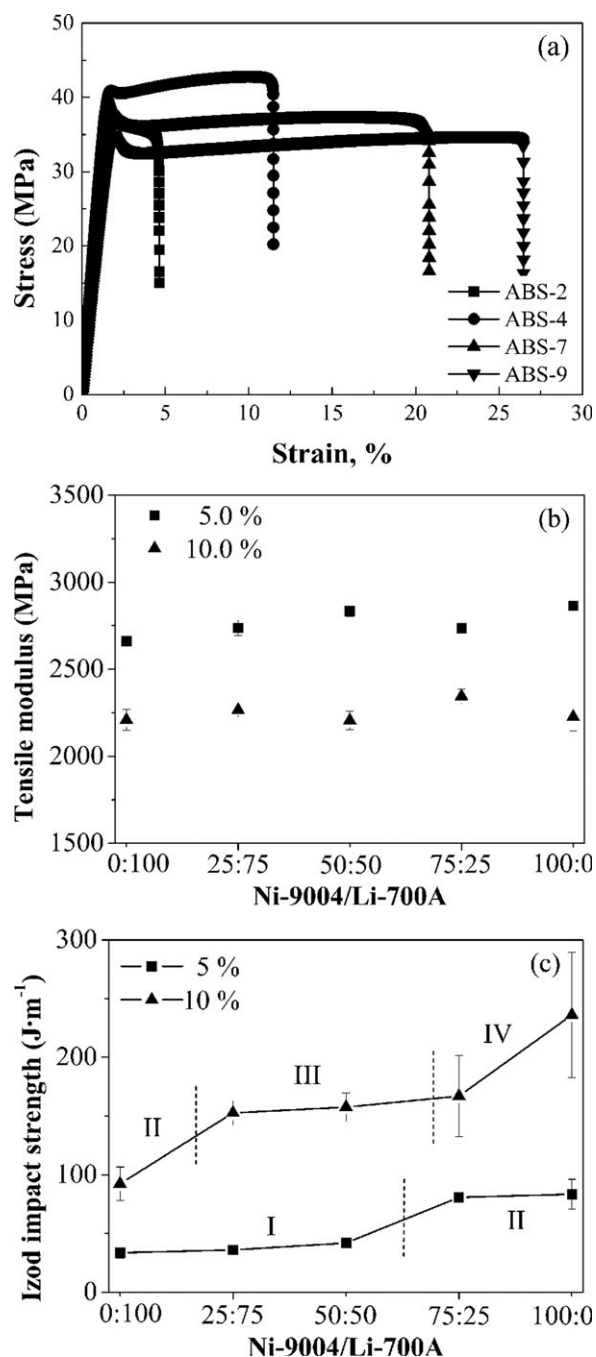
Figure 2. Stress–strain curves (a), tensile moduli (b), and notched Izod impact strengths (c) of ABS with various rubber contents.

Moreover, the dramatic differences between those f–t curves indicate quite different fracture mechanisms. Take ABS-2 as an example [Figure 3(a)], the stress on specimen derived from the hammer concentrates at its notch tip during crack initiation, but it is too low to enable crack propagation.[24] As a result, it exhibits brittle fracture characterized by an approximately linear and sharp loading curve and a limited and insufficient plastic deformation, ending in an abrupt drop after reaching F_{max}. As far as semiductile test piece (e.g., ABS-4) is concerned, a large increase of propagation energy is absorbed and semiductile tear-

ing mechanism is exhibited. The specimen is characterized by typical elastic–plastic behavior dominated by unstable crack propagation where the impact force keeps invariant transitorily and then gradually reduces to zero. The plateau broader than that of ABS-2 at the maximum of f–t curve is due to plastic deformation visible as circumferential stress whitened area on the specimen surface. In contrast, the ductile (ABS-7) and super-tough specimen (ABS-9) show a stable crack growth mechanism, and the plastic deformation tends to be more evidently and the transported force drops very slowly to zero or a certain value above zero within the total deflection, respectively.

All in all, under instrumented impact tests, brittle or semiductile material performs relatively higher F_0 and F_{max} and lower t_{max} and d_{max} values; for ductile or super-tough material, the relatively smaller F_0 and F_{max} and higher t_{max} and d_{max} values are presented. These great differences are ultimately attributed to the enhanced strength and stiffness of the former, compared to the latter, whose ductility and resistance against stable crack propagation are increased besides a decreased flexural modulus and yield strength.[25,26]

On the other hand, though there exist controversies about defining explicitly the crack initiation point,[2,24,27] Hristov's opinion is adopted in our evaluations that assume the crack propagation stage begins just at F_{max} of f–t curve.[28] So, the overall fracture process during impact can be divided into two stages—crack initiation and crack propagation stages, and correspondingly, the initiation energy (W_i) and propagation energy (W_p) as energy portions measured up to F_{max} and from F_{max} to full fracture of specimen, respectively, can be obtained through the integral treatment of f–t curves. The characteristic energies determined in the instrumented impact tests are analyzed and summarized in Figure 4. The calculated W_0/W_t, W_i/W_t, and W_p/W_t are the rates of inertial energy, initiation energy, and propagation energy portions to total energy absorbed in the fracture process, respectively.

As can be seen from the bar graph, remarkably, for 5.0 wt % of total rubber usage, W_0 accounts for about 35.0% of the total energy and becomes smaller with enhancing total rubber usage and Ni-9004 amount blended [Figure 4(a)]. It can be concluded that as for quasi-brittle material, though inertial peak does not occupy a predominant position, it plays an important role in the whole fracture process, whereas it can be negligent for semi-ductile or ductile materials due to its extremely small contribution to the failure mechanism. Viewing from the columnar section in Figure 4(b), an approximately analogous tendency of W_i/W_t with improving the total rubber usage and Ni-9004 amount in compounded rubber can be obtained. It indicates that during the fracture initiation stage, a considerable amount of impact energy (up to > 80.0% of W_t) is dissipated and absorbed for 5.0 wt % rubber usage, compared to the higher rubber fraction (10.0 wt %), at which the material reveals high plasticity and low elasticity (the maximum W_i/W_t is only 50.0%). However, W_p/W_t is quite the contrary to the former two parameters and greatly enhanced by the total content of rubber [Figure 4(c)]. The fracture propagation stage at higher rubber fraction shows less variation and dominates in the whole
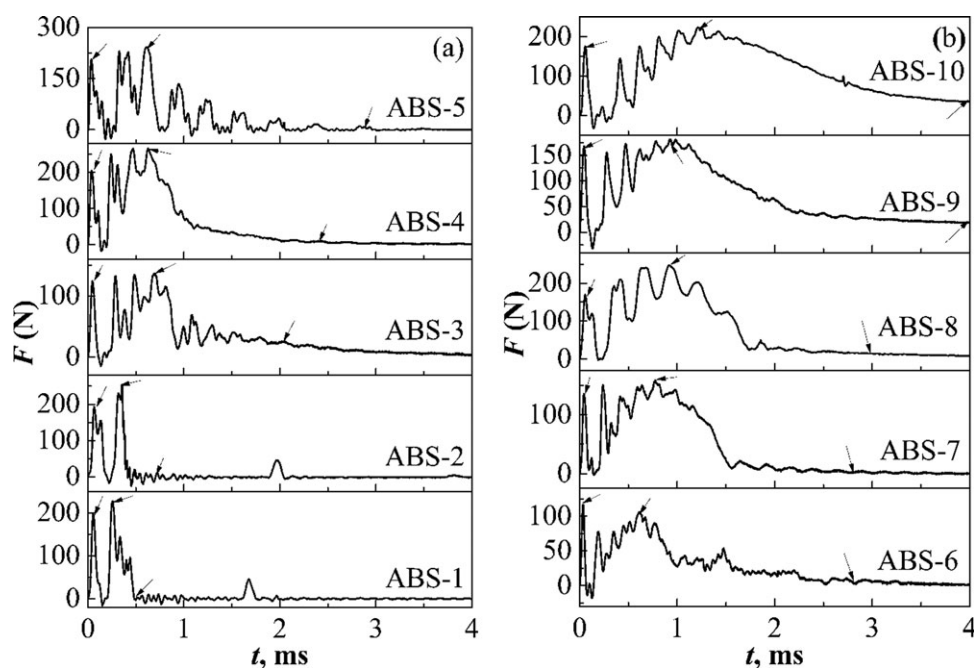
Figure 3. Typical *f–t* curves recorded during instrumented impact tests of ABS specimens with different usage of compounded rubbers: (a) 5.0 wt % and (b) 10.0 wt %.

failure progress compared with that at lower rubber usage. Figure 4(d) shows the ductility index, W_p/W_i, as a function of different rubber level and mixing ratio. Similar to W_p/W_t, W_p/W_i also increases basically with an increase in rubber usage and Ni-9004/Li-700A ratio, demonstrating stable crack growth and much more energy absorbed during crack propagation region rather than crack initiation region.

Fractography and Fracture Mechanism
To better understand the failure process behavior and mechanism, the fracture surfaces of typical failed specimens during instrumented impact tests were examined using SEM. All the directions of the applied impact load and fracture extend from top to bottom in each SEM photograph. To facilitate the discussion, all of the fracture surfaces were observed under different magnifications in three different zones (shown in Figure 5): (i) very close to the notch edge, (ii) midsection, and (iii) near to the boundary.

Figure 6(a, b) shows the overall morphologies of ABS-2 specimen. As presented in Figure 6(c), it can be observed that near to the notch position, the pronounced molten state and stretching phenomena occur, which are the results of adiabatic shearing effect. The existence of flake structures about 0.6 mm away from the notch edge indicates that the obvious plasticization under shearing takes place due to the plane-stress put on specimen. This area is corresponding to the descent stage of inertial peak in the *f–t* curve. In the deflection range of 0.6–1.8 mm, the fracture surface seems relatively smooth. However, under a larger magnification (10,000×), a great deal of densely distributed cavitation (<70 nm), naked rubber particles (70–3300 nm), and matrix stripping can be clearly identified [Figure 6(d)], which are beneficial to dissipate impact energy and thus

promote craze slowly developing to crack. The plastic deformation is also related to rubber particle cavitation.[29]

Furthermore, ahead of crack initiation zone, there are a few secondary crack sources (breakup points) caused by rupture of polymer chains in the central section of Figure 6(e). Simultaneously, a great many river-pattern fibrous stripes spread along the impact direction originating from those breakup points. Besides, the intermolecular chains slip and debond; as a result, the irregular peeling patterns around the boundary are induced by swift crack propagation. Those results support the previous findings by Yu et al. who concluded that slippage and separation of PS crazes occurred accompanying with debonding and brittly rupturing of polymer material on the craze interface.[30] Meanwhile, the periodical stripes (Wallner lines, at the arrow)

Table II. Force–Time Curve Parameters in Impact Tests on ABS Terpolymers

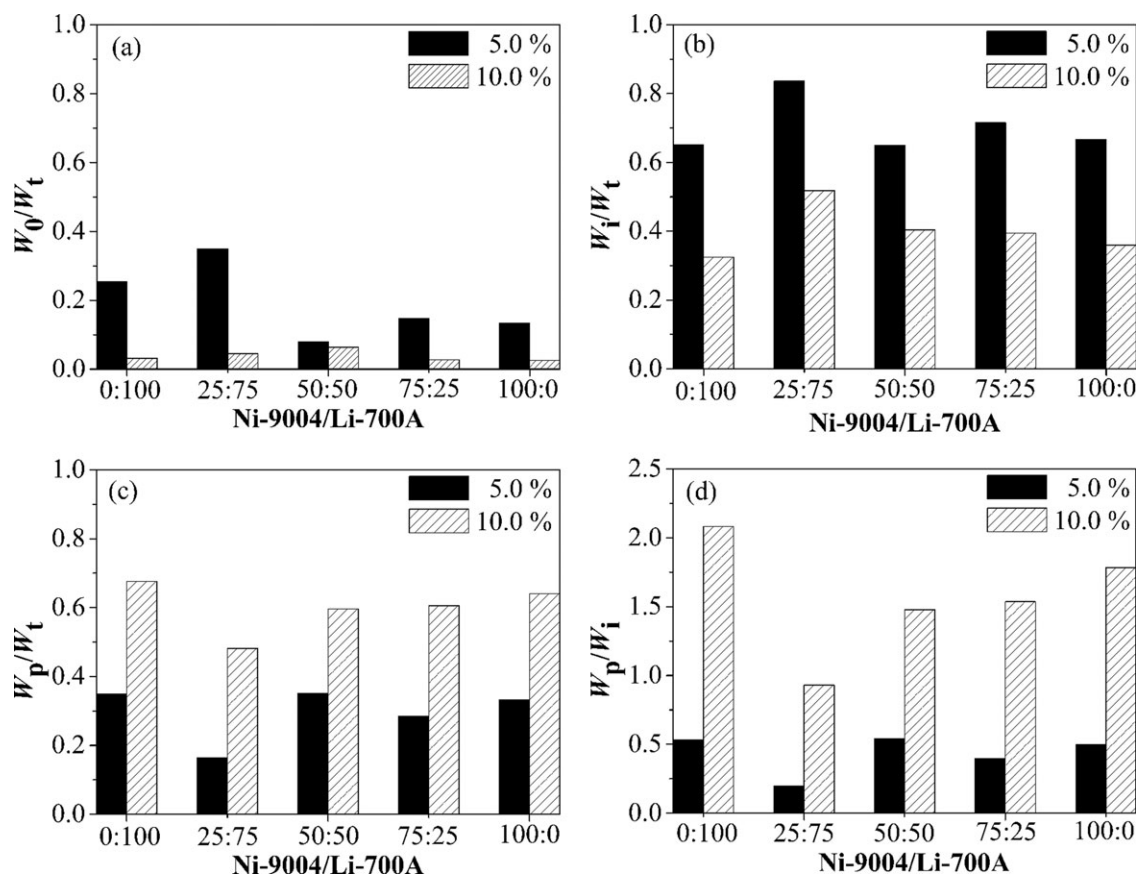| Sample	F_0 (N)	t_{max} (ms)	d_{max} (mm)	F_{max} (N)	W_{max} (J)	W_t (J)
ABS-1	193.2	0.34	1.17	236.1	0.09	0.15
ABS-2	195.4	0.33	1.13	260.4	0.11	0.16
ABS-3	183.7	0.55	1.53	239.2	0.12	0.26
ABS-4	198.0	0.62	2.10	269.1	0.16	0.29
ABS-5	183.9	0.61	2.06	245.5	0.21	0.39
ABS-6	117.3	0.69	2.37	121.5	0.12	0.46
ABS-7	132.1	0.69	2.37	162.0	0.20	0.74
ABS-8	143.5	0.72	2.44	158.4	0.24	0.76
ABS-9	166.6	0.79	2.67	171.1	0.32	0.96
ABS-10	170.7	0.91	4.08	223.8	0.53	1.33

Figure 4. W_0/W_t (a), W_i/W_t (b), W_p/W_t (c), and W_p/W_i (d) of toughened ABS with various rubber ratio and usage.

are also presented in the bilateral sections of Figure 6(a), which are resulted from the superposition action of elastic stress waves. Those results are related to the elastic accumulation energy and formed biggish crazes.[31] Clearly, the characterless bands and the peeling bands alternate and become denser and denser with the crack propagation. At the same time, their dimensions decrease gradually. These results can be well explained by a diminishing impact force with crack propagation [Figure 3(a)]. Finally, a blunting zone in Figure 6(f) appears close to the end of fracture surface, where stress response varies from tension to compression status. Polymer crazes swiftly develop and rupture associated with the plasticization phenomenon (stress-whitening) strongly dependent on compressive stress.

The total morphologies of ABS-4 specimen are displayed in Figure 7(a, b). Compared with ABS-2, ABS-4 shows more evident shear lips around the notch tip and cavities (1.5–4.0 μm) with or without occlusions in front of the tip [Figure 7(c)], demonstrating an outstanding plasticization under strong shearing and much more rubber particles easily separating or drawn from matrix due to its relatively lower GD and Nt* (Table I). Figure 7(d) reveals that in the crack initiation zone, a mass of ligulalike structures and crazing phenomena (stress-whitening) are developed and produced, and the plastic deformation of matrix and cavitation of rubber particles are the main fracture mechanisms.

Followed that, the formed parabolic shape morphology on the upper part of Figure 7(e) (arrow position) can be ascribed to

the far higher propagation velocity of the main cracks than that of the secondary cracks. During the process of deformation and cavitation, considerable impact energy is consumed and dissipated. As a result, the propagation velocity of main crack is restricted; while it is reduced and comparable to the level of secondary crack, firework type and divergent patterns emerge in the lower part of Figure 7(e) (vertical arrows). Besides, when both kinds of cracks spread in variant velocity, the impact force dramatically falls, whereas it drops gradually when their speed is comparable [Figure 3(a)]. After undergoing a mirror zone with no characteristics, the fracture progress enters the crack fast-
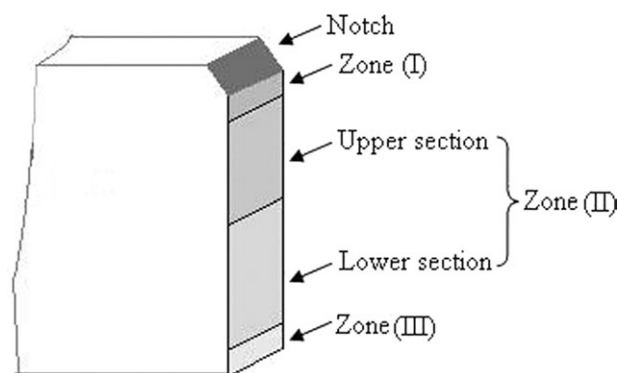

Figure 5. Schematic diagram of different portions of the fracture surface where the morphologies were observed.
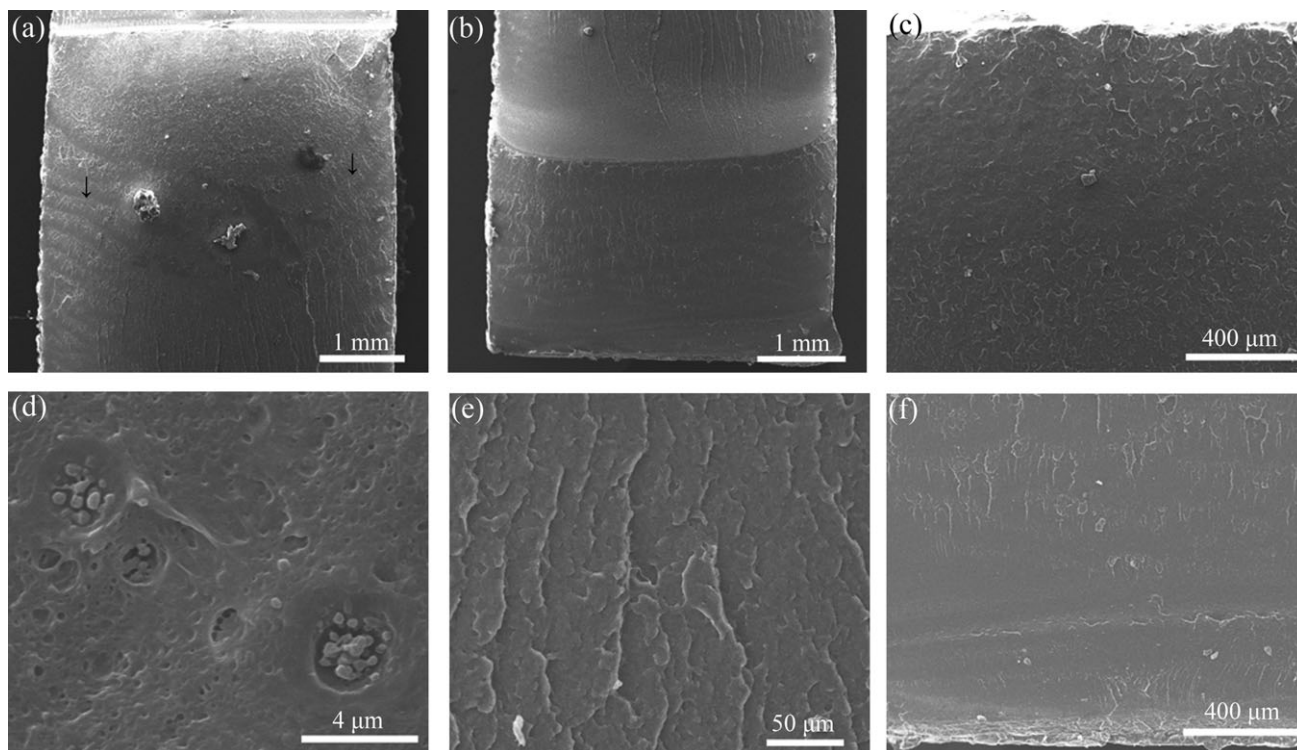
Figure 6. Photomicrographs of the fracture surface of ABS-2: (a) upper half section, (b) lower half section, (c) zone I, (d) upper section of zone II, (e) lower section of zone II, and (f) zone III.
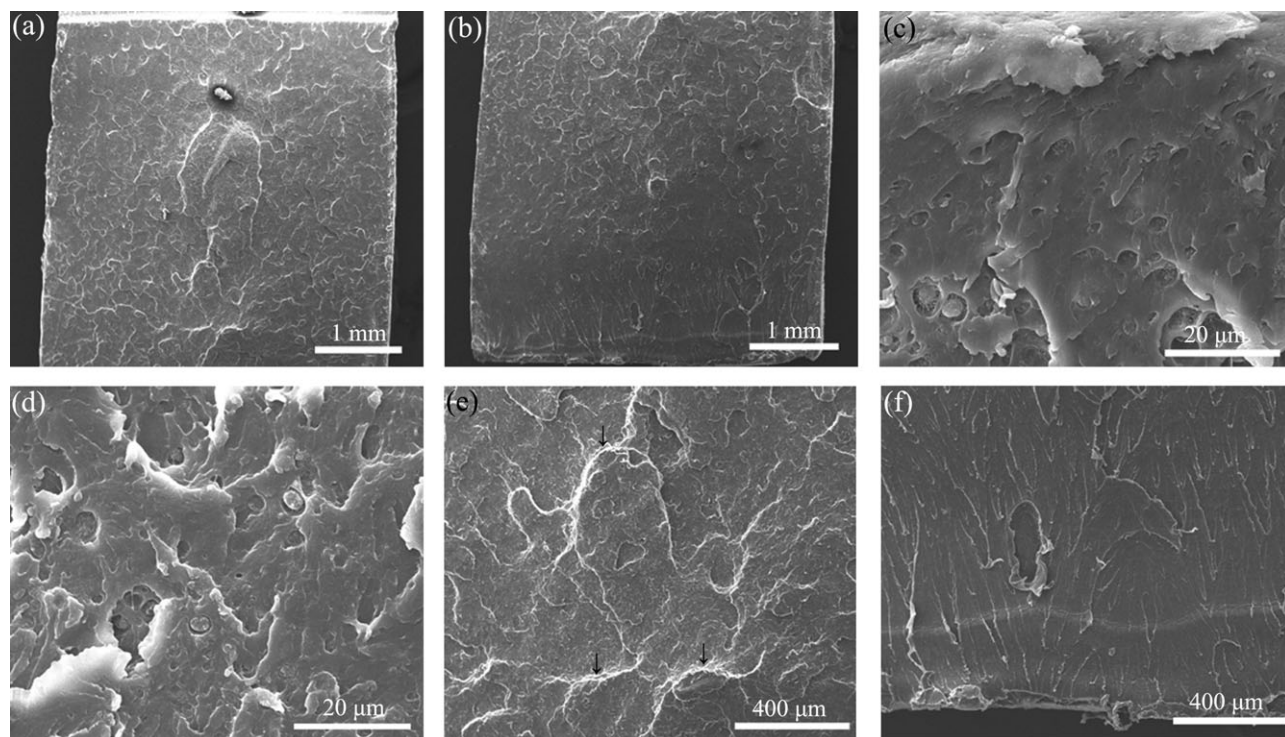

Figure 7. Photomicrographs of the fracture surface of ABS-4: (a) upper half section, (b) lower half section, (c) zone I, (d) upper section of zone II, (e) lower section of zone II, and (f) zone III.
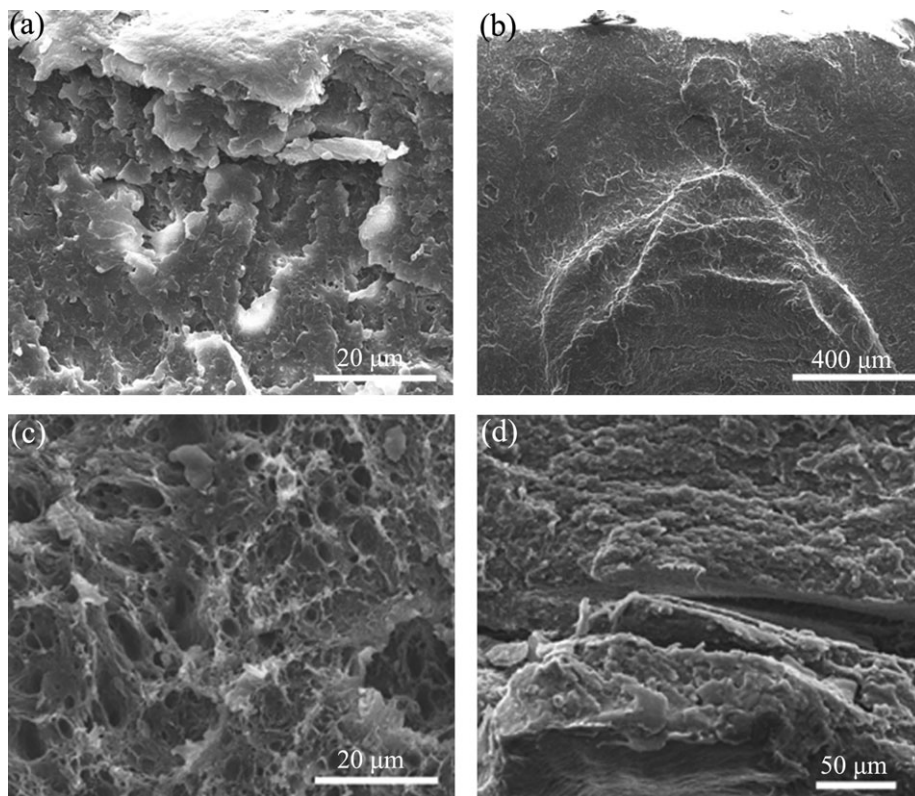
Figure 8. Photomicrographs of the fracture surface of ABS-7: (a) zone I, (b) upper section of zone II, (c) lower section of zone II, and (d) zone III.
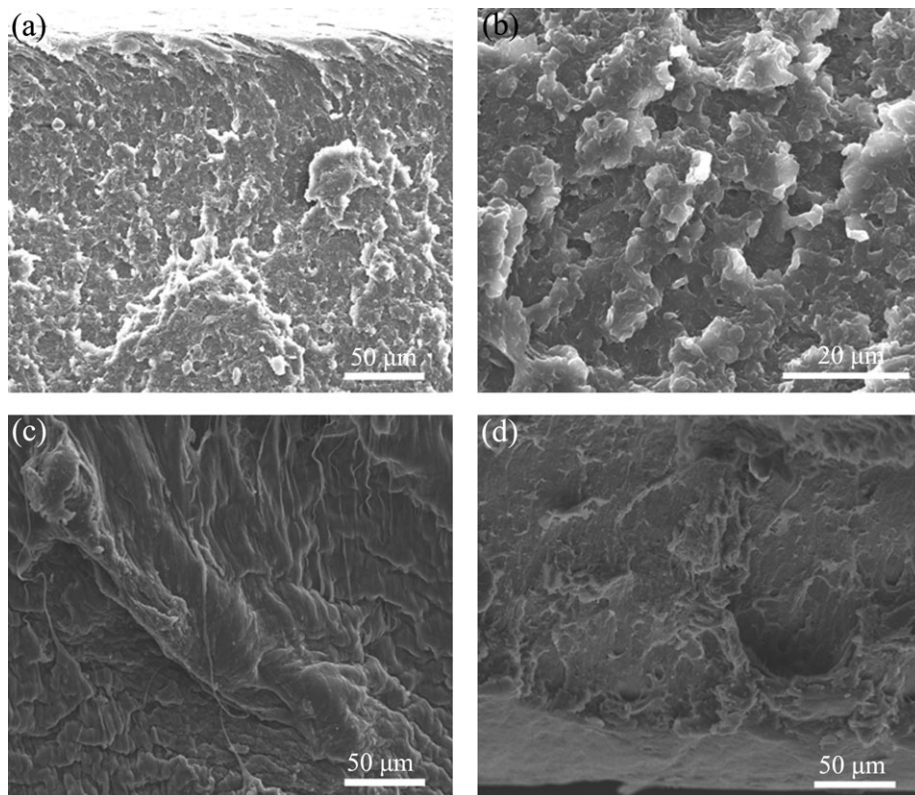

Figure 9. Photomicrographs of the fracture surface of ABS-9: (a) zone I, (b) upper section of zone II, (c) lower section of zone II, and (d) zone III.

spreading area. As illustrated in Figure 7(f), many long white pinstripes with branching and curling boundary stretch to the blunting zone along the impact direction.

ABS-7, a representative of ductile fracture mode, displays a rougher and more uneven fracture surface near to the notch edge [(Figure 8(a)]. Plasticization, minute pores, and microsized cavities are attributed to the adiabatic shearing, smaller Li-700A particles apart from matrix, and larger Ni-9004 particles in connection with partial resins peeling off from the surrounding matrix, respectively. On the other hand, because of the synergistic effect of various sized rubber particles, many parabolic shapes with a large number of fine crazes initiating and developing are overlapped and elongated [Figure 8(b)]. However, the overlapping and interleaving stress fields surrounding the rubber particles lead to more and more concentrated stress and ultimately, the bursting of large bulk matrix and the beginning of rupture. And then, as shown in Figure 8(c), the network structure and cavitations present, which signify the deformation, orientation and ductile yielding of rubber particles. Furthermore, stress-whitening and ligulalike structures are still distinct, expressing ductile yielding and ligament-forming being the main deformation mechanisms. In the end, an obvious stress blunting zone is formed because of the state of stress response. Lots of previously grown fibrous crazes aggregate and extend continuously [Figure 8(d)]. Some cease at the edge of blunting zone and the others run through the zone and keep on developing.

In contrast, ABS-9 exhibits super-high toughness and presents hinge-fracture mode in impact test (the specimen was partially fractured and the output force signal at the maximal deflection in Figure 3(b) is approximately 20.0 N and far greater than zero). Figure 9(a, b) shows much more ligulalike structures without accompanying cavitation outlining stress-whitening caused by the ductile tearing and orientation of ligament when the external force exerting on specimen. Moreover, the apparent shear yielding and the melt-flowing lacertuses also appear in the related fractogram [Figure 9(c)]. In summary, these results imply that the crack bowing and deflection, shear yielding, debonding, and ductile tearing of ligament are the main toughening mechanisms at higher rubber content and Ni-9004 composition. It is exactly these special structures making the propagation of crazes and cracks effectively restrained. As a result, the crack propagation is forced to change direction, to slow down, and to defuse energy, and therefore, the material shows a super ductile fracture mode and has relatively higher Izod impact strength [Figure 2(c)].

CONCLUSIONS

Various ABS terpolymers were prepared by mass grafting copolymerization using two PB rubbers and their composite types as toughener. Their morphology, mechanical performances, and fracture behavior were investigated. As for the structure–property relationship, materials with larger particles or more Ni-9004 amount show better tensile and impact properties. The *f*–*t* diagrams can be regarded as a criterion for evaluating crack propagation and failure mechanisms through various

parameters. Fractography displays that quasi-brittle fracture occurs accompanied by pronounced cavitation and matrix stripping coupled with riverlike fibrous and periodical Wallner stripes; as for ductile fracture, alternate parabolic and firework patterns followed by stress-whitening and ligaments are obviously exhibited.

REFERENCES

1. van der Wal, A.; Nijhof, R.; Gaymans, R. J. *Polymer* **1999**, *40*, 6031.

2. Li, D. W.; Li R. K. Y.; Tjong, S. C. *Polym. Test.* **1997**, *16*, 563.

3. Grellmann W.; Lach, R. *Appl. Macromol. Chem. Phys.* **1997**, *253*, 27.

4. Rogers, M. G.; Plumtree, A. *Polym. Test.* **1992**, *11*, 13.

5. Karger-Kocsis, J. *J. Appl. Polym. Sci.* **1992**, *45*, 1595.

6. Tai, C. M.; Li, R. K. Y.; Ng, C. N. *Polym. Test.* **2000**, *19*, 143.

7. Pick, L. T.; Harkin-Jones, E. *J. Mater.: Des Appl.* **2005**, *219*, 1.

8. Arici, A.; Sinmazçelık, T.; Çapan, L.; Yilgör, İ.; Yilgör, E. *J. Compos. Mater.* **2005**, *39*, 21.

9. Okada, O.; Keskkula, H.; Paul, D. R. *J. Polym. Sci. Polym. Phys.* **2004**, *42*, 1739.

10. Cheon, S. S.; Lim, T. S.; Lee, D. G. *Compos. Struct.* **1999**, *46*, 267.

11. Pickett, A. K.; Pyttel, T.; Payen, F.; Lauro, F.; Petrinic, N.; Werner, H.; Christlein J. *Int. J. Impact. Eng.* **2004**, *30*, 853.

12. Duan, Y.; Saigal, A.; Greif, R.; Zimmerman, M. A. *Polym. Eng. Sci.* **2003**, *43*, 112.

13. Han, Y.; Lach, R.; Grellmann, W. *Appl. Macromol. Chem. Phys.* **1999**, *270*, 13.

14. Yu, Z.; Li, Y.; Zhao, Z.; Wang, C.; Yang, J.; Zhang, C.; Li, Z.; Wang, Y. *Polym. Eng. Sci.* **2009**, *49*, 2249.

15. Yu, Z.; Li, Y.; Wang, Y.; Yang, L.; Liu, Y.; Li, Y.; Li, Z.; Zhao, Z. *Polym. Eng. Sci.* **2010**, *50*, 961.

16. Hayes, R. A.; Futamura, S. J. Polym. Sci. Polym. Chem. Ed. **1981**, *19*, 985.

17. Sohn, S.; Kim, S.; Hong, S. I. *J. Appl. Polym. Sci.* **1996**, *61*, 1259.

18. Yang, J.; Wang, C.; Yu, Z.; Li, Y.; Yang, K.; Wang, Y. *J. Appl. Polym. Sci.* **2011**, *121*, 2458.

19. Kuhn, R.; Müller, H. G.; Bayer, G.; Krämer-Lucas, H.; Kaiser, W.; Orth, P.; Eichenauer, H.; Ott, K. H. *Colloid Polym. Sci.* **1993**, *271*, 133.

20. Díaz de León, R.; Morales, G.; Acuňa, P.; Soriano, F. *Polym. Eng. Sci.* **2010**, *50*, 373.

21. Jose, S.; Thomas, S.; Lievana, E.; Karger-Kocsis, J. *J. Appl. Polym. Sci.* **2005**, *95*, 1376.

22. Thomas, S.; Groeninckx, G. *Polymer* **1999**, *40*, 5799.

23. van der Wal, A.; Verheul, A. J. J.; Gaymans, R. J. *Polymer* **1999**, *40*, 6057.

24. Chang, L.; Zhang, Z.; Breidt, C. *Appl. Compos. Mater.* **2004**, *11*, 1.

25. van der Wal, A.; Mulder, J. J.; Gaymans, R. J. *Polymer* **1998**, *39*, 5477.

26. Bucknall, C. B.; Karpodinis, A.; Zhang, X. C. *J. Mater. Sci.* **1994**, *29*, 3377.

27. van der Wal, A.; Mulder, J. J.; Thijs, H. A.; Gaymans, R. J. *Polymer* **1998**, *39*, 5467.

28. Hristov, V. N.; Lach, R.; Grellmann, W. *Polym. Test.* **2004**, *23*, 581.

29. Adhikari, R.; Lach, R.; Michler, G. H.; Weidisch, R.; Grellmann, W.; Knoll, K. *Polymer* **2002**, *43*, 1943.

30. Yu, J.; Jin, Z. H.; Zhou, H. J. *J. Chin. Electron. Microsc. Soc.* **1993**, *4*, 324.

31. Xiao, L. C.; Li, Z. Z.; Du, L. Y. *Polym. Mater. Sci. Eng.* **1990**, *4*, 61.